

Article

# Formation of Tubular Carbonates within the Seabed of the Northern South China Sea

Yuedong Sun <sup>1,2,3,4,5</sup> , Jörn Peckmann <sup>3</sup> , Yu Hu <sup>6</sup> , Xudong Wang <sup>6</sup>, Shanggui Gong <sup>6</sup>, Yongbo Peng <sup>6</sup>, Duofu Chen <sup>2,6</sup> and Dong Feng <sup>2,6,\*</sup> 

- <sup>1</sup> Key Laboratory of Ocean and Marginal Sea Geology, South China Sea Institute of Oceanology, Innovation Academy of South China Sea Ecology and Environmental Engineering, Chinese Academy of Sciences, Guangzhou 510301, China; ydsun@scsio.ac.cn
  - <sup>2</sup> Laboratory for Marine Mineral Resources, Qingdao National Laboratory for Marine Science and Technology, Qingdao 266061, China; dfchen@shou.edu.cn
  - <sup>3</sup> Institute for Geology, Center for Earth System Research and Sustainability, Universität Hamburg, 20146 Hamburg, Germany; joern.peckmann@uni-hamburg.de
  - <sup>4</sup> Southern Marine Science and Engineering Guangdong Laboratory (Guangzhou), Guangzhou 511458, China
  - <sup>5</sup> University of Chinese Academy of Sciences, Beijing 100049, China
  - <sup>6</sup> Shanghai Engineering Research Center of Hadal Science and Technology, College of Marine Sciences, Shanghai Ocean University, Shanghai 201306, China; huyu@shou.edu.cn (Y.H.); xdwang@scsio.ac.cn (X.W.); sggong@shou.edu.cn (S.G.); ybpeng@nju.edu.cn (Y.P.)
- \* Correspondence: dfeng@shou.edu.cn

Received: 1 August 2020; Accepted: 28 August 2020; Published: 29 August 2020



**Abstract:** A remarkable exposure of tubular authigenic carbonates was found on the seafloor in the Dongsha area of the South China Sea (SCS). The tubular carbonates, around 2–3 cm in diameter and usually less than 10 cm in length, represent broken fragments of once-larger pipes that now protrude from muddy sediments. The morphology, carbon and oxygen stable isotope compositions, and trace and rare earth element contents of the carbonates were analyzed to decipher the mode of carbonate formation. The tubular carbonates exhibit a dark brown coating of iron and manganese hydrous oxides, indicating prolonged exposure to oxic bottom waters. The carbonate content of the micritic pipes falls between 12.5 and 67.3 wt.% with an average of 42.0 wt.%, suggesting formation within the sediment. This inference is supported by trace and rare earth element patterns including a moderate enrichment of middle rare earth elements. Low  $\delta^{13}\text{C}$  values (as low as  $-50.3\text{‰}$ , Vienna Pee Dee Belemnite (VPDB)) suggest that carbonate precipitation was induced by the anaerobic oxidation of methane. The unusually positive  $\delta^{18}\text{O}$  values of the carbonates (as high as  $+5.3\text{‰}$ , VPDB) are believed to reflect the destabilization of locally abundant gas hydrate. Taken together, it is suggested that pipe formation was initiated by sediment-dwelling organisms, such as crustaceans or bivalves. The burrows subsequently acted as conduits for upward fluid migration. The lithification of the sediment directly surrounding the conduits and the partial filling of the conduits with carbonate cement resulted in the formation of tubular carbonates. Turbidity currents, sediment slumps, or the vigorous emission of fluids probably induced the fragmentation of tubular carbonates within the sediment. The carbonate fragments had been further subjected to winnowing by bottom currents. This study provides insight into the interaction of megafauna burrowing with fluid migration and carbonate formation at hydrocarbon seeps, highlighting the role of bottom currents and mass wasting on the formation of fragmented tubular carbonates.

**Keywords:** methane seep; tubular carbonate; sediment slump; bottom current; South China Sea

## 1. Introduction

The discharge of hydrocarbon-rich fluids from marine sediments has been widely recognized along active and passive continental margins worldwide [1]. The elevated alkalinity in pore waters resulting from the anaerobic oxidation of methane (AOM) induces the precipitation of carbonate minerals close to the seafloor [2,3]. The morphologies of such seep carbonates are various, including slabs, crusts, mounds, and highly irregular bodies [4–11]. Tubular, cylindrical carbonates have also been commonly described [11–13]. Tubular carbonates exhibit various sizes but are typically some centimeters in diameter and a few decimeters in length (e.g., [9,13]). Some tubular carbonates, however, are up to 5 m in length and up to 1 m in diameter [14]. They are typically hosted within sediments in a vertical or subvertical position [15]. Tubular carbonates form within the sediment but sometimes are exhumed, leaving the pipes scattered on the seafloor (e.g., [16]).

Formation mechanisms for tubular carbonates have been proposed, including (i) tubeworm fossilization, (ii) the lithification of subsurface sediment around fluid conduits such as burrows or fractures, and (iii) chimneys projecting into seawater (e.g., [5,9,10,14,17]). Tubular carbonates surrounding tubeworm fossils typically exhibit small diameters (less than 1 cm; [18]). Larger tubular carbonates, particularly those with diameters above 1 m, likely represent the subsurface plumbing systems of ancient seeps [14], enabling fluid flux over long distances upward through the sedimentary column. Many of the carbonate pipes found at seeps, typically several centimeters in diameter, derive from the cementation of burrows produced by the local megafauna (e.g., [9]).

Isolated tubular carbonates have been reported at only a few seeps in the northern South China Sea (SCS; [19–21]). In the summer of 2018, a research cruise involving a remotely operating vehicle (ROV) ROPOS explored the continental slope of the northern SCS. At a seep site at about 700 m water depth, an extensive exposure of tubular carbonate fragments scattered on the seafloor was discovered. Here, the morphology, carbon and oxygen stable isotope, and element analyses of these samples were performed to elucidate the mode of carbonate formation. We further discuss the possible processes involved in the formation of the tubular carbonates.

## 2. Geological Setting

The SCS, a marginal sea connected to the west Pacific Ocean by the Luzon Strait, is located at the junction of three plates, the Eurasian, Indian–Australian, and Pacific plates [22]. A series of sedimentary basins (i.e., the Qiongdongnan Basin, Pearl River Mouth Basin, and Taixinan Basin) is located in the northern SCS, where the northeastern passive continental margin reaches a sedimentary cover of up to 10 km in thickness (Figure 1; [23]). The NE Dongsha area is situated in the southwestern Taiwan Basin. Well-developed fault systems and mud diapirs serve as conduits for hydrocarbon migration [19,24–26]. A gas hydrate drilling expedition confirmed the occurrence of gas hydrate and authigenic seep carbonate in this region [27].

Seep carbonates were first discovered in this area in 2004 [19,28]. In the same year, different types of seep carbonates were discovered in this area during the Sino-German joint cruise *SO 177* [19,29]. Many carbonate rock and biological samples, the latter including bivalves, tubeworms, gastropods, and corals, were collected during this cruise using TV-guided grabs [19,29]. The local seafloor morphology is characterized by deep-cutting, NW–SE-trending canyons [30]. Abundant mud volcanoes, scarps, sediment slumps, and slides are developed in this area [19,24,25].

The study area is characterized by a complex hydrography (Figure 1). Oceanographic and geologic observations provide evidence for the intrusion of the Northern Pacific Deep Water (NPDW) into the SCS through the Luzon Strait, a situation that has existed at least since the early Quaternary based on sedimentary records (Figure 1; [31–33]). A series of sediment waves and sedimentary drifts on the continental slope of the Dongsha area indicates the existence of a strong deep-water bottom current derived from the NPDW [32,34,35]. Additionally, the Luzon Strait is well known for its intense internal tides [36], which are generated in the Luzon Strait and then propagate into the SCS [36–38]. The near-bottom breaking of the internal waves may result in the generation of along-slope currents in

the study area [38]. The internal tides have been observed to cause the resuspension and redistribution of bottom sediment [38,39]. To sum up, the existence of strong bottom and along-slope currents causes a dynamic hydrographic environment in the study area.

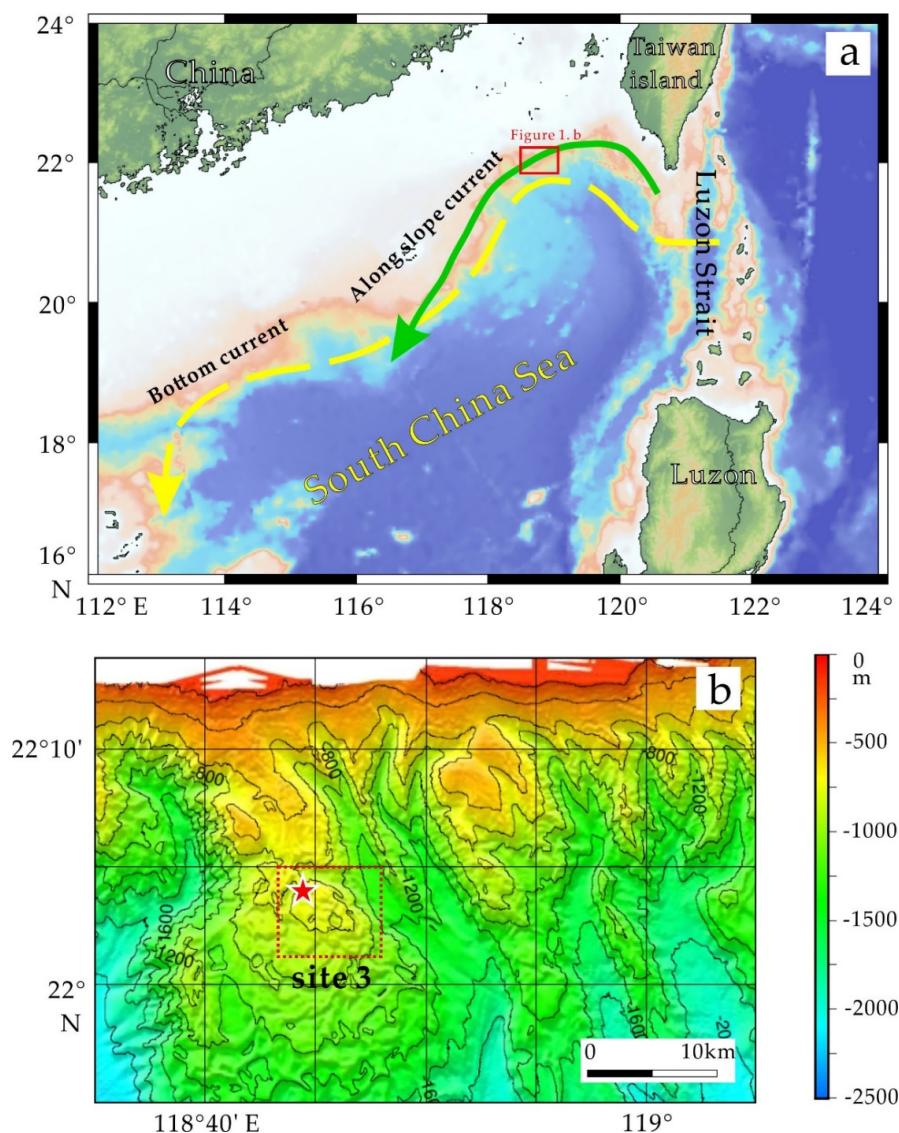


**Figure 1.** The topography of the northern South China Sea and the regional setting of the study area. (a) Deepwater-bottom-current and along-slope-current data are taken from Liu et al. [31] and Xie et al. [38]. Base map was created by using GeoMapApp. (b) Sample locations of tubular carbonates in this study (red star); bathymetric map from [19]. The red dotted rectangle indicates the location of Site 3.

### 3. Materials and Methods

During the *Tan KaH Kee* Cruise in summer 2018, ROV ROPOS was used to conduct seafloor observation and sampling of Site 3 [19,29] of the Dongsha area (Figure 1). Tubular carbonate fragments and seafloor sediment were sampled at the southern end of the ridge ( $22^{\circ}4.0563' N$ ,  $118^{\circ}44.7869' E$ ) at a water depth of about 700 m (Figure 1b), using a net attached to the manipulator arm of the ROV ROPOS during dive 2073 (Figures 2 and 3). The carbonates were washed with fresh water after collection and were subsequently air-dried. Before sub-sampling, iron and manganese hydrous oxides coatings on the surface of carbonates were removed with a dental drill, and then, carbonates were

broken into small pieces and placed in an ultrasonic deionized-water bath for 20 min. The samples were placed in a thermostat container (40 °C) for 24 h. The samples were ground into powder using an agate mortar for element analyses.

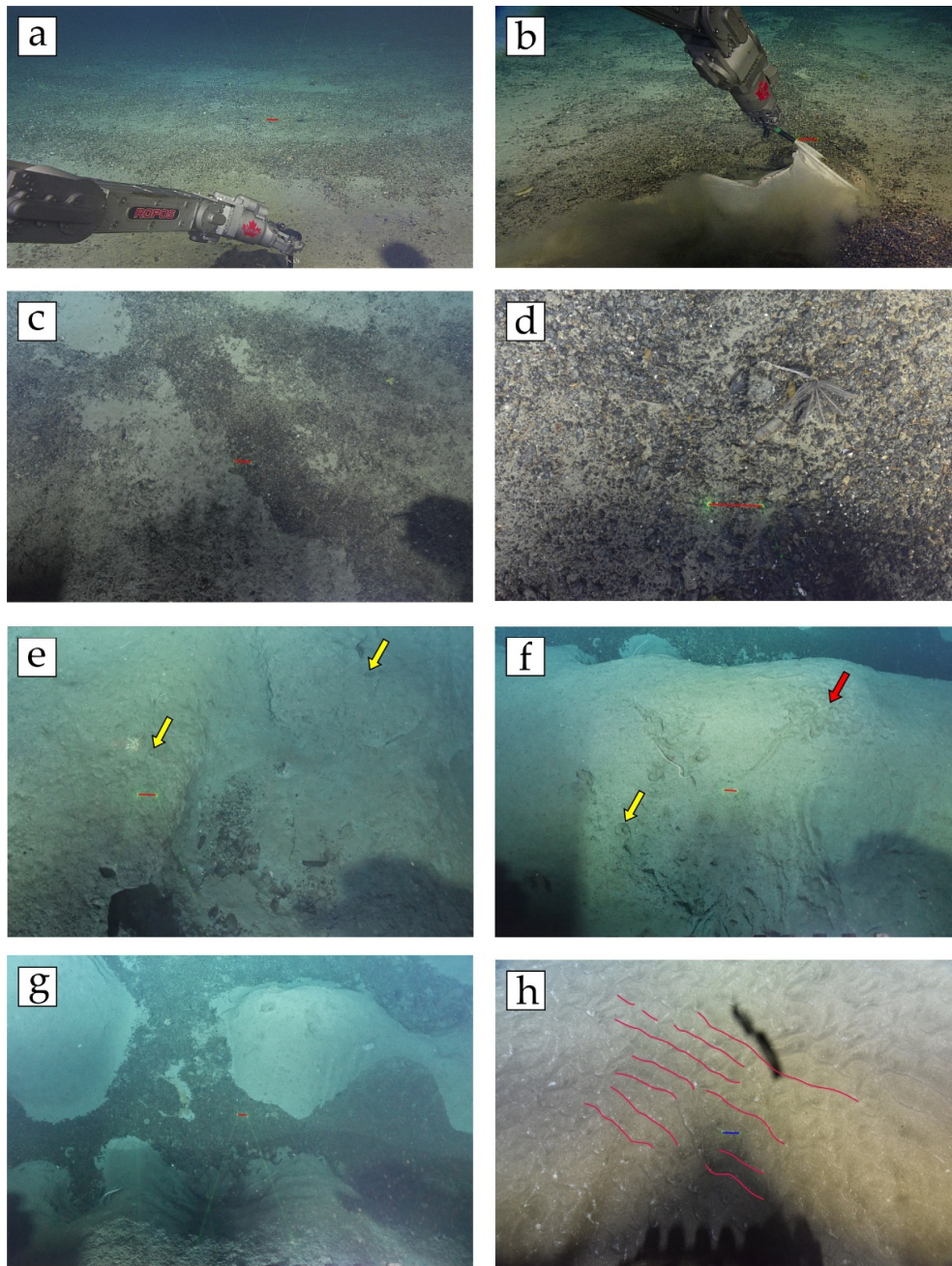


**Figure 2.** Seafloor images of sampling location. (a) Exposure of fragments of tubular carbonates on the seafloor. (b) The studied samples were collected using the manipulator arm of the ROV ROPOS. (c,d) Close-up of tubular carbonate fragments on the seafloor. (e) Some tubular carbonates were buried within sediment mounds (yellow arrows). (f) Numerous carbonate fragments in the depression between sediment mounds. (g) Suspected traces of biological activity on the surface of a sediment mound (red arrow), and a tubular carbonate buried within sediment (yellow arrow). (h) Current ripples in the study area. The widths of the colored short lines bounded by green dots are about ten centimeters.

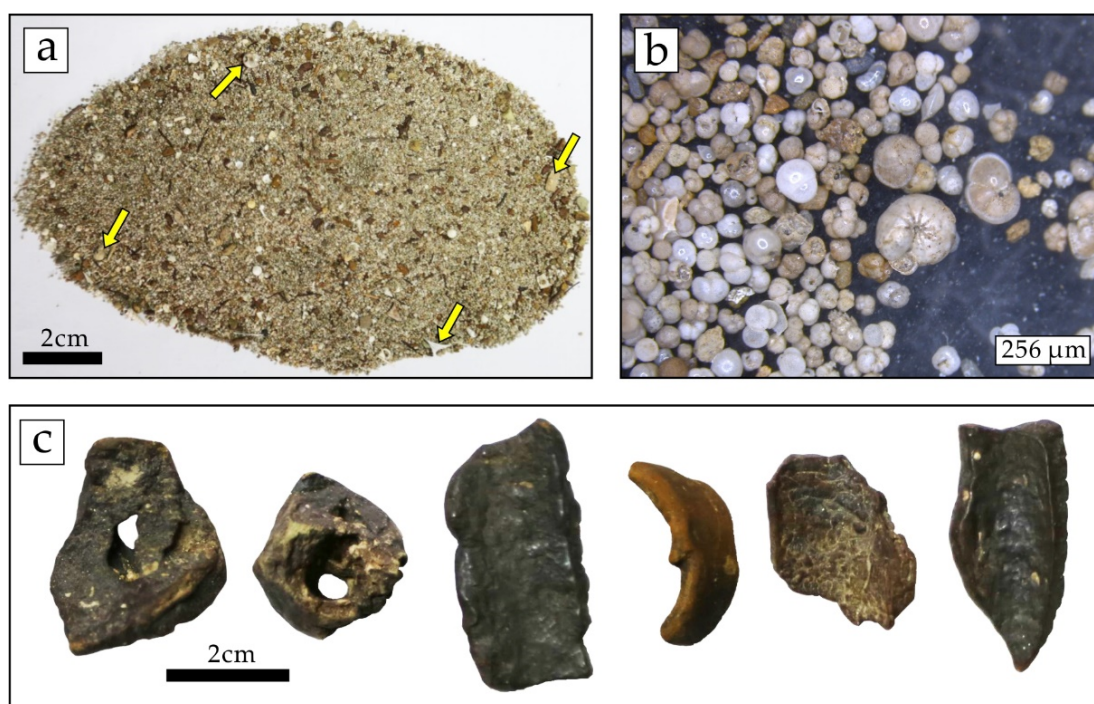


**Figure 3.** Samples collected from the study area. (a) Surface sediment sampled along with tubular carbonate fragments on the seafloor. Note the abundant small carbonates and bioskeletal fragments (yellow arrows). (b) Sediment rich in foraminifera. (c) Fragments of tubular carbonates. Note the extensive coatings of iron and manganese hydrous oxides on the surface of the samples.

### 3.1. Carbonates' Carbon and Oxygen Stable Isotopes

The powders were sampled with a microdrill for carbon and oxygen stable isotope analysis. The samples were measured with a Thermo Finnigan Delta V Advantage mass spectrometer at Louisiana State University. Released  $\text{CO}_2$  for isotope analysis was processed with pure phosphoric acid (90 °C). The results are reported in per mil (‰) using the  $\delta$  notation relative to the Vienna Pee Dee Belemnite (VPDB) standard ( $\delta^{13}\text{C}$  and  $\delta^{18}\text{O}$ ). The long-term standard deviation was smaller than 0.06‰ for  $\delta^{13}\text{C}$  values and 0.08‰ for  $\delta^{18}\text{O}$  values.

### 3.2. Major and Trace Elements of Bulk Rocks

Approximately 50 mg amounts of powdered samples were dissolved with a mixture of 1 mL of HF (48%, *v/v*) and 1 mL of  $\text{HNO}_3$  (68%, *v/v*) in cleaned Teflon beakers. The samples were then placed into an electric oven at 185 °C overnight; the solution was evaporated to dryness on a hot plate. After cooling, a mixture of 2 mL of  $\text{HNO}_3$  (68%, *v/v*) and 3 mL of deionized water together with a Rh spike (200 ppb) was added into the beakers. The beakers were placed in an electric oven again at 135 °C for 5 h to dissolve the residue. An aliquot of the solution was transferred into cleaned Teflon vials for trace element analysis. Finally, another aliquot of the solution together with a Cd spike (200 ppm) was poured into acid-cleaned vials for major element analysis.

### 3.3. Major and Trace Elements of Carbonate Phases

Approximately 20 mg amounts of powders were weighed into cleaned centrifuge tubes and leached with ultra-pure 5% acetic acid for 2 h to dissolve the carbonate phases. The tubes were then centrifuged at 3500 rpm for 4 min, and the supernatants were transferred into cleaned Teflon beakers and evaporated to dryness. The dried residues were dissolved with 5%  $\text{HNO}_3$  again. Finally, an aliquot of the solution was transferred into cleaned vials together with a Rh spike (10 ppb) for REE analysis.

Another aliquot of the solution with a Rh spike (200 ppb) was poured into cleaned vials for major element analysis.

The elemental contents of the bulk rocks and carbonate phases were analyzed at the State Key Laboratory of Ore Deposit Geochemistry, Chinese Academy of Sciences. Major and trace elements were analyzed with a Varian Vista Pro ICP-AES and a Plasma Quant MS ICP-MS, respectively. Certified reference materials (OU-6, AMH-1, and GBPG-1) were used for quality control. The precision and accuracy were both better than 5% for major elements and 10% for trace elements.

In this paper, the REE contents were normalized against Post Archaean Average Shale (PAAS) [40]. The subscript “N” denotes shale-normalized values. In order to rule out the effect of La overabundance, the real Ce anomalies were quantified by comparing Pr/Pr\* with Ce/Ce\* following the method of Bau and Dulski [41]. The elemental anomalies were calculated as follows  $Ce/Ce^* = 3Ce_N/(2La_N + Nd_N)$ ,  $Pr/Pr^* = 2Pr_N/(Ce_N + Nd_N)$ , and  $La/La^* = La_N/(3Pr_N - 2Nd_N)$ .

## 4. Results

### 4.1. Seafloor Observations

According to the ROV observations, abundant tubular carbonates were lying on the seafloor (Figure 2a–d). The original lengths of tubular carbonates cannot be determined due to their severe fragmentation. Some tubular carbonates were buried within sediment pingoes (Figure 2e,f; yellow arrows). Suspected traces of biological activity were discovered on the surface of sediment mounds (Figure 2f). Carbonate fragments were found to be particularly abundant in the depressions around sediment mounds (Figure 2e–g). The best-preserved tubular carbonates have a cylindrical shape, are 2 to 3 cm in diameter, and are up to 10 cm in length (Figure 2e). In addition, current ripples are widely distributed in the study area (Figure 2h). The sediments collected from the seafloor include abundant small carbonates and bioskeletal fragments (Figure 3a). The local coarse-grain seafloor sediment is rich in foraminifera, most of which are larger than 60  $\mu\text{m}$  (Figure 3b). Many of the tubular carbonates display hollow central conduits, generally less than 2–3 cm in diameter (Figure 3c). The external surface of the tubular carbonates is coated by black to dark brown iron and manganese hydrous oxides (Figure 3c).

### 4.2. Elemental Contents of Bulk Rocks and Carbonate Phases

Selected major and trace-elemental contents of bulk rocks and carbonate phases are listed in Table 1. The calcium contents (CaO, wt.%) of the bulk rock vary from 1.6% to 32.3% (average:  $15.3\% \pm 8.3\%$ ,  $n = 10$ ). The tubular carbonates (bulk) show low magnesium contents (MgO), ranging from 2.0% to 6.9% (average:  $4.2\% \pm 1.5\%$ ,  $n = 10$ ). Except for two samples, most of the bulk samples have low strontium contents ranging from 126 to 497  $\mu\text{g/g}$  (average:  $337 \pm 113 \mu\text{g/g}$ ). The bulk rocks display high Mg/Ca and low Sr/Ca ratios (Table 1; Figure 4). The manganese contents of the carbonate phase range from 490.4 to 1146.5  $\mu\text{g/g}$  (average:  $722.7 \pm 209.5 \mu\text{g/g}$ ). The carbonate phase exhibits variable strontium contents spanning from 60 to 5140  $\mu\text{g/g}$  and low Mn/Sr ratios falling between 0.1 and 3.9 (average:  $2.0 \pm 1.3$ ), with one outlier of 10.6.

### 4.3. Carbon and Oxygen Stable Isotopes of Carbonates

The  $\delta^{13}\text{C}$  values of the tubular carbonate fragments are exclusively negative (Figure 5; Table S1 (Supplementary Material)), spanning from  $-50.3\text{‰}$  to  $-29.0\text{‰}$  (mean =  $-40.5\text{‰}$ , SD =  $7.3\text{‰}$ ,  $n = 13$ ). The  $\delta^{18}\text{O}$  values of the samples range from  $1.8\text{‰}$  to  $5.3\text{‰}$  (mean =  $3.6\text{‰}$ , SD =  $1.1\text{‰}$ ,  $n = 13$ ).

**Table 1.** Selected elemental contents of carbonate phases and bulk rocks.

Sample ID	Bulk Sample						Carbonate Phase		
	CaO	MgO	Carb. cont. <sup>1</sup>	Sr	Mg/Ca	Sr/Ca	Sr	Mn	Mn/Sr
	%	%	%	µg/g	wt./wt.	wt./wt.	µg/g	µg/g	wt./wt.
C1	11.9	4.4	36.5	353	0.310	0.004	293	875.4	3.0
C2	12.5	6.9	46.5	355	0.467	0.004	291	1146.5	3.9
C3	21.0	6.0	58.7	477	0.241	0.003	458	533.7	1.2
C4	20.2	5.8	56.5	497	0.242	0.003	483	502.7	0.1
C5	32.3	2.7	67.3	4760	0.071	0.021	5140	883.1	1.8
C6	22.5	2.0	47.3	4680	0.075	0.029	4920	490.4	0.1
C7	11.6	4.3	35.7	406	0.307	0.005	382	921.8	2.4
C8	1.6	2.7	12.5	126	1.432	0.011	60	639.9	10.6
C9	9.7	3.2	28.3	248	0.276	0.004	195	657.7	3.4
C10	9.2	4.0	30.6	307	0.368	0.005	267	575.6	2.2

<sup>1</sup> Carb. cont. = mean carbonate content = CaCO<sub>3</sub> + MgCO<sub>3</sub>.

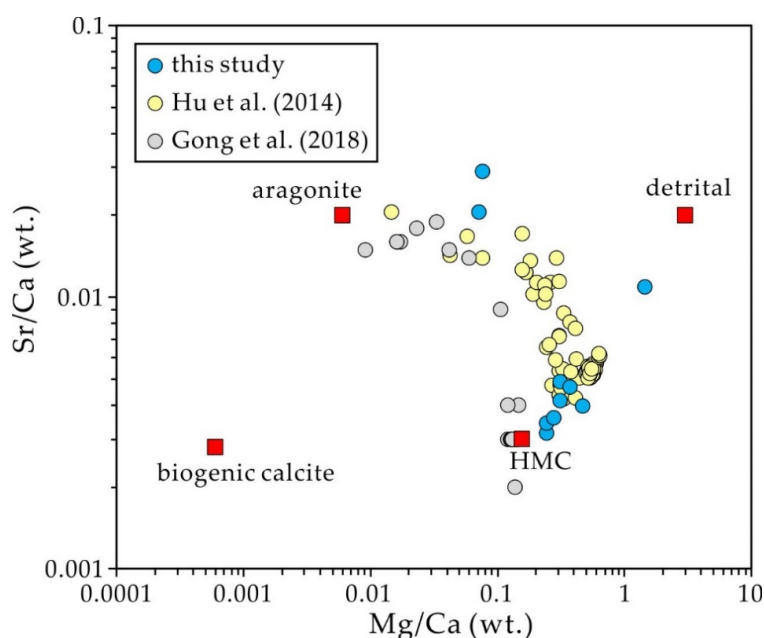


**Figure 4.** Relationship between Sr/Ca and Mg/Ca (wt. ratio) of carbonate samples. The end members of the Sr/Ca and Mg/Ca ratios were 0.020 and 0.0063 for aragonite and were 0.0031 and 0.155 for high magnesium calcite (HMC), respectively; data from Gong et al. [42]. The end-member ratios of the biogenic calcite and the detrital fraction are from Yang et al. [43].

#### 4.4. Rare Earth Elements

Table 2 presents the REE contents in the carbonate phase of the studied samples. The carbonates show intermediate to high total REE contents ( $\Sigma$ REE), ranging from 23.2 to 47.0 µg/g (average =  $32.9 \pm 6.0$  µg/g). The carbonate phases display similar REE patterns: (1) middle REE (MREE) enrichment relative to light REE (LREE) and heavy REE (HREE; average  $Gd_N/Yb_N = 1.48 \pm 0.24$ ); (2) LREE depletion (average  $Pr_N/Yb_N = 0.72 \pm 0.34$ ); (3) pronounced negative Ce and slightly positive La anomalies (Figure 6; average  $Ce/Ce^* = 0.70 \pm 0.06$ ;  $La/La^* = 1.37 \pm 0.10$ ); (4) low Y/Ho ratios between 28.1 and 34.6 with an average of  $31.3 \pm 1.7$  (Table 2).

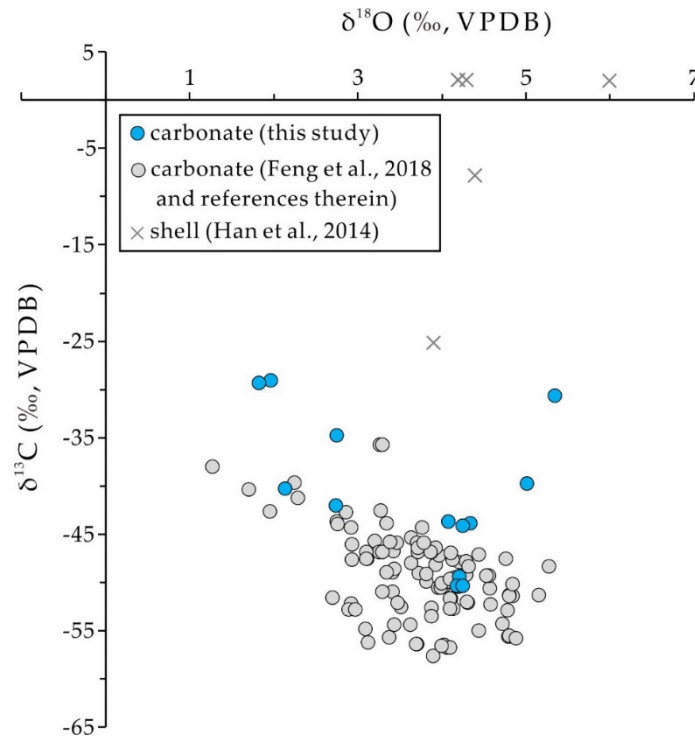


**Figure 5.** Cross plot of  $\delta^{13}\text{C}$  and  $\delta^{18}\text{O}$  values of carbonates and shells (published data for this site are from Feng et al. [30] and references therein).

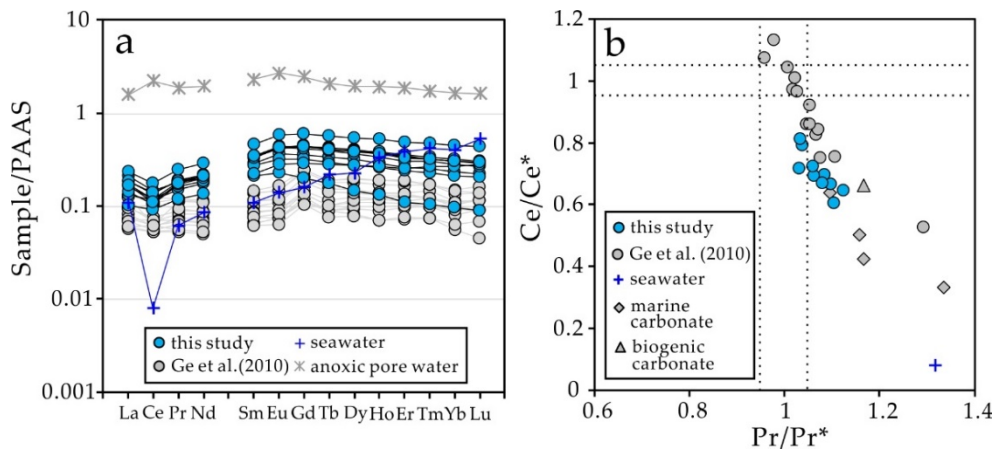


**Figure 6.** Shale-normalized REE patterns and plot of  $\text{Pr}/\text{Pr}^*$  versus  $\text{Ce}/\text{Ce}^*$  of tubular carbonates. (a) The fragments of tubular carbonate have REE patterns similar to those of the samples of Ge et al. [44] but are different from those of seawater ( $\times 10^6$ ) and anoxic pore water ( $\times 10^6$ ) [45–47]. (b) Plot of  $\text{Pr}/\text{Pr}^*$  versus  $\text{Ce}/\text{Ce}^*$  used to reveal Ce anomalies of the studied samples [41]. The fragments of tubular carbonate display negative Ce anomalies, which are similar to those of seawater, biogenic carbonate, and non-seep marine carbonates (data from [46,48]).

**Table 2.** Rare earth element compositions ( $\mu\text{g/g}$ ) of tubular carbonates from the northern South China Sea.

Sample Number	C1	C2	C3	C4	C5	C6	C7	C8	C9	C10
La	6.2	5.0	7.1	8.0	8.9	6.6	5.4	3.9	7.0	6.4
Ce	9.4	9.1	10.8	11.7	13.8	9.4	8.2	7.3	11.0	8.7
Pr	1.6	1.3	1.7	1.6	2.2	1.4	1.5	1.0	1.6	1.6
Nd	7.1	5.9	7.3	6.8	9.7	6.3	6.7	4.6	7.1	7.1
Sm	1.9	1.6	1.9	1.5	2.6	1.2	1.8	1.2	1.9	1.9
Eu	0.5	0.4	0.5	0.3	0.6	0.2	0.5	0.3	0.5	0.5
Gd	2.0	1.7	2.0	1.5	2.8	0.9	1.9	1.4	2.1	2.0
Tb	0.3	0.3	0.3	0.2	0.4	0.1	0.3	0.2	0.3	0.3
Dy	1.9	1.5	1.8	1.3	2.5	0.7	1.7	1.3	1.9	1.8
Ho	0.4	0.3	0.4	0.3	0.5	0.1	0.3	0.3	0.4	0.4
Er	1.0	0.7	0.9	0.7	1.4	0.3	0.9	0.7	1.0	0.9
Tm	0.1	0.1	0.1	0.1	0.2	0.0	0.1	0.1	0.1	0.1
Yb	0.9	0.7	0.8	0.6	1.3	0.3	0.8	0.8	0.9	0.9
Lu	0.1	0.1	0.1	0.1	0.2	0.0	0.1	0.1	0.1	0.1
Y	12.0	9.0	11.5	8.3	16.2	3.6	9.8	7.8	13.2	11.3
$\Sigma\text{REE}$	33.3	28.5	35.7	34.6	47.0	27.5	30.2	23.1	35.9	32.7
Y/Ho	32.4	31.8	31.3	32.3	31.6	28.1	29.4	29.7	34.6	31.5
La/La*	1.34	1.29	1.32	1.52	1.45	1.42	1.27	1.26	1.36	1.52
Ce/Ce*	0.66	0.79	0.69	0.72	0.69	0.67	0.64	0.81	0.72	0.60
Pr/Pr*	1.10	1.04	1.09	1.03	1.06	1.08	1.12	1.03	1.06	1.10
Dy <sub>N</sub> /Sm <sub>N</sub>	1.16	1.08	1.12	1.00	1.18	0.69	1.09	1.23	1.16	1.12
Pr <sub>N</sub> /Yb <sub>N</sub>	0.59	0.59	0.59	0.59	0.59	0.59	0.59	0.59	0.59	0.59
Gd <sub>N</sub> /Yb <sub>N</sub>	1.44	1.44	1.44	1.44	1.44	1.44	1.44	1.44	1.44	1.44

## 5. Discussion

### 5.1. Constraints on the Formation Environment of Tubular Carbonates

The carbonate mineralogy, stable isotope characteristics ( $\delta^{13}\text{C}_{\text{carb}}$  and  $\delta^{18}\text{O}_{\text{carb}}$ ), and REE patterns of carbonates can be used to constrain the fluid sources and formation environments (e.g., [30,49,50]). The carbonate mineralogy of rocks can be constrained by the Mg/Ca and Sr/Ca ratios of whole rocks [42,51,52]. According to the concept of Bayon et al. [51], high-magnesium calcite (HMC) is the main carbonate mineral phase of the studied samples (Figure 4). In contrast to the dominance of dolomite cement in most extant and ancient tubular carbonates (e.g., [53–56]), the dominance of HMC in the studied samples may be ascribed to an incomplete consumption of sulfate in pore water or concentrations of sulfide not high enough to catalyze dolomite formation [57,58]. In addition, tubular carbonates show low carbonate contents (Table 1) and contain abundant detrital quartz and feldspar [59]. Therefore, tubular carbonates originally precipitated in an anoxic environment within the sediment column.

Compared to the  $\delta^{13}\text{C}$  values of shells collected from the same area [20], the extremely low  $\delta^{13}\text{C}$  values ( $-50.3\text{‰}$ ; Figure 5) of the authigenic carbonate pipes indicate biogenic methane as the dominant carbon source for carbonate precipitation [3]. This interpretation is supported by the isotope composition of methane from a neighboring site, varying from  $-72.3\text{‰}$  to  $-69.4\text{‰}$  [60]. Tarutani et al. [61] reported that  $10^3\ln_{\alpha}^{18}\text{O}_{\text{calcite-water}}$  will increase by  $0.06\text{‰}$  with each mol% of  $\text{MgCO}_3$  incorporated into the crystal lattice. Assuming the tubular carbonates formed at current temperature ( $6.7\text{ °C}$ , CTD data) and the HMC contains 20 mol%  $\text{MgCO}_3$  [59], according to Equation (1), the calculated  $\delta^{18}\text{O}$  values of the fluids from which the carbonate precipitated are  $+2.6\text{‰}$  VSMOW, using the  $\delta^{18}\text{O}$  values of the analyzed samples [62].

$$10^3\ln_{\alpha}^{18}\text{O}_{\text{calcite-water}} = 18.03 (10^3/T) - 32.42 \quad (T \text{ is degrees Kelvin}) \quad (1)$$

Such positive  $\delta^{18}\text{O}_{\text{carb}}$  values reflect the addition of  $^{18}\text{O}$ -rich fluids (e.g., [4,63]). The dominance of biogenic methane suggests a shallow source, where temperature and pressure conditions are insufficient for the dehydration of clay minerals. The local occurrence of methane hydrate indicates that the  $^{18}\text{O}$ -enriched fluid was derived from hydrate decomposition (e.g., [60,64]).

The rare earth element patterns of seep carbonates have been used to constrain the diagenetic conditions under which authigenesis took place [49,65–68]. The lack of a good correlation between the total REE ( $\Sigma\text{REE}$ ) and Fe and Mn contents (Figure S1 (Supplementary Material)) suggests that the dissolution of iron and manganese hydrous oxides has no significant effect on REE patterns. The lack of linear relationships between Ce anomalies and  $\text{Dy}_\text{N}/\text{Sm}_\text{N}$ ,  $\Sigma\text{REE}$  (Figure S2 (Supplementary Material)), and low Mn/Sr ratios (Table 1) in our samples render significant diagenetic alteration unlikely. Therefore, the studied carbonate fragments are likely to preserve the composition of pore water. The  $\Sigma\text{REE}$  contents of the tubular carbonates are in the same orders of magnitude as those of other seep carbonates (Figure 6a; e.g., [28,44,65,67,69,70]). All the studied samples display similar shale-normalized REE patterns (except for sample C6), suggesting precipitation under similar conditions (Figure 6a). The REE patterns reflect slight enrichment of HREEs ( $\text{Pr}_\text{N}/\text{Yb}_\text{N} = 0.7 \pm 0.2$ ), pronounced cerium anomalies ( $\text{Ce}/\text{Ce}^* = 0.7 \pm 0.0$ ; Figure 6b), and slight lanthanum anomalies ( $\text{La}/\text{La}^* = 1.4 \pm 0.1$ ). At first glance, these patterns reflect the pore fluids from which carbonates precipitated, apparently strongly influenced by oxygenated seawater (Figure 6a). However, the moderate MREE enrichment ( $\text{Gd}_\text{N}/\text{Yb}_\text{N} = 1.5 \pm 0.2$ ) and low Y/Ho ratios ( $31.3 \pm 1.7$ ; Table 2) disagree with a strong influence of oxygenated seawater during carbonate precipitation. MREE enrichment can be explained by the reduction of iron and manganese hydrous oxides in anoxic sediment [71]. Previous studies reported that anoxic pore water at seeps is typified by MREE enrichment (Figure 6a; [45,72]).

Given that AOM requires strictly anoxic conditions, it is difficult to understand why the tubular carbonates exhibit pronounced negative Ce anomalies (Figure 6). Negative Ce anomalies in oxygenated seawater result from the microbial oxidation of  $\text{Ce}^{3+}$  followed by the preferential scavenging of  $\text{Ce}^{4+}$  [73]. The presence of negative Ce anomalies in seep carbonates has been ascribed to intermittent oxygenation during carbonate formation [65,69,74,75]. Alternatively, one study suggested that negative Ce anomalies and the HREE enrichment of seep carbonates may reflect high porewater alkalinity [67]. Considering the overall high alkalinity in pore waters at seeps, it is feasible that a combination of high alkalinity and organic matter content in pore water resulted in the negative Ce anomalies and HREE enrichment of the studied samples.

## 5.2. Mode of Tubular Carbonate Formation

Tubular carbonates characterized by a large diameter (particularly  $>1$  m) have been regarded as a product of ancient seafloor plumbing systems [14,76]. In contrast, tubular carbonates derived from the lithification of tubeworms have much smaller diameters (typically a few millimeters; [18]). Complex carbonate towers projecting into the water column are mainly composed of fibrous aragonite cement, including examples from the Black Sea, the eastern Mediterranean Sea, and the oxygen minimum zone in the Arabian Sea (e.g., [5,8]).

Considering the morphology (diameter  $> 2$  cm; Figures 2 and 3) of tubular carbonates, the lack of tubeworm fossils in the carbonates, and the scarcity of tubeworms in the study area, the studied samples are unlikely to represent the residues of worm tubes (e.g., [10,11,77,78]). Burrows generated by seep-dwelling macrobenthos (bivalves and crustaceans) can act as fluid migration pathways for focused methane seepage [10,79–82]. The studied tubular carbonates are best interpreted as the result of carbonate precipitation within burrows and preceding lithification of the surrounding sediment caused by the precipitation of methane-derived microcrystalline carbonate [9]. However, we are unable to determine the type of organism that generated the burrows. Abundant bivalve shells were discovered at the study site, and bivalves are also abundant at a neighboring active methane seep (e.g., [19,29,30]). In addition, crustaceans were also found among the mussel beds of a neighboring

methane seep, including galatheid crabs and shrimp [30]. To sum up, the studied tubular carbonates most likely represent the cemented burrows of seep-dwelling benthos (i.e., bivalves or crustaceans).

The precipitation of tubular carbonates occurred in a restricted environment within the sediment column. Some tubular carbonates were vertically or sub-vertically orientated within the sediment. The exposure of dense accumulations of fragments of tubular carbonates on the seafloor and the presence of iron and manganese hydrous oxide coatings indicate exhumation by strong bottom currents and the alteration of pipe surfaces by oxidized seawater. In addition to hydrographic characteristics, the local frequency of mass-wasting processes (turbidity currents and sediment slumps) may have been favorable for the exhumation of tubular carbonates. Finally, vigorous methane emissions caused by the decomposition of gas hydrate that occurred in the study area during times of falling or low sea levels (cf. [55]) may have contributed to the exhumation of carbonate pipes.

In our scenario, methane seeps provided nourishment for lush megafauna, which produced numerous burrows in the unconsolidated host sediment (Figure 7a). At the time of burrowing activity or slightly later, burrows acted as conduits for fluid discharge (Figure 7b). AOM occurred within the burrows and the surrounding sediments, generating high alkalinity that induced the lithification of the surrounding sediments (Figure 7b). The dissociation of gas hydrate generated substantial quantities of methane gas that generated localized overpressure. The sediment pingoes discovered in the study area likely resulted from the accumulation of sediment on the seafloor due to the expulsion of mixtures of water, gas, and solid materials (Figure 2f,g; [83]). The fragmentation of tubular carbonates took place during or after exhumation, probably involving mass-wasting processes (Figure 7c). The strong local deep-water bottom currents developed in the study area [32,34,35] likely contributed to exhumation, but it is unknown if they contributed to fragmentation too. Bottom currents generated from the near-bottom breaking of internal waves have velocities as high as 77 cm/s [35,38]. The coarse-grain foraminifera-rich sediment possibly reflects winnowing by such high-velocity bottom currents. However, the possibility that the foraminifera-rich sediment derived from turbidity currents cannot be ruled out either. Finally, the observed current ripples possibly provide further evidence for strong bottom currents or turbidity currents. Accordingly, mass-wasting processes and strong bottom currents are potential mechanisms for the exhumation and fragmentation of tubular carbonates, the latter also preventing their burial (Figure 7d; [84–86]). After exhumation, exposure to oxic seawater led to the precipitation of iron and manganese hydrous oxides on the surface of carbonates (Figure 7d). Similar scenarios for the exposure of carbonate pipes have been put forward for occurrences in other regions, such as the Montenegro Margin [15], the Gulf of Cadiz [16], and the Stirone River locality [84].

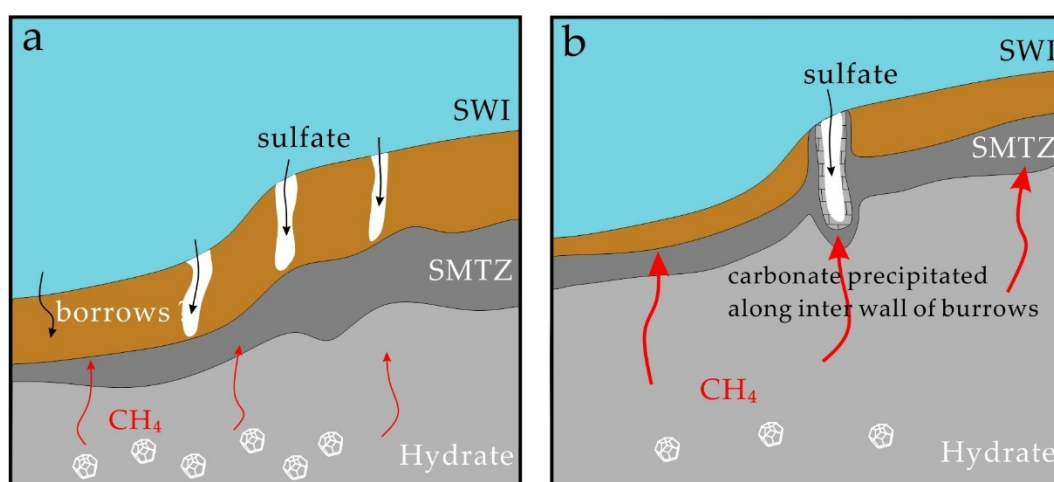
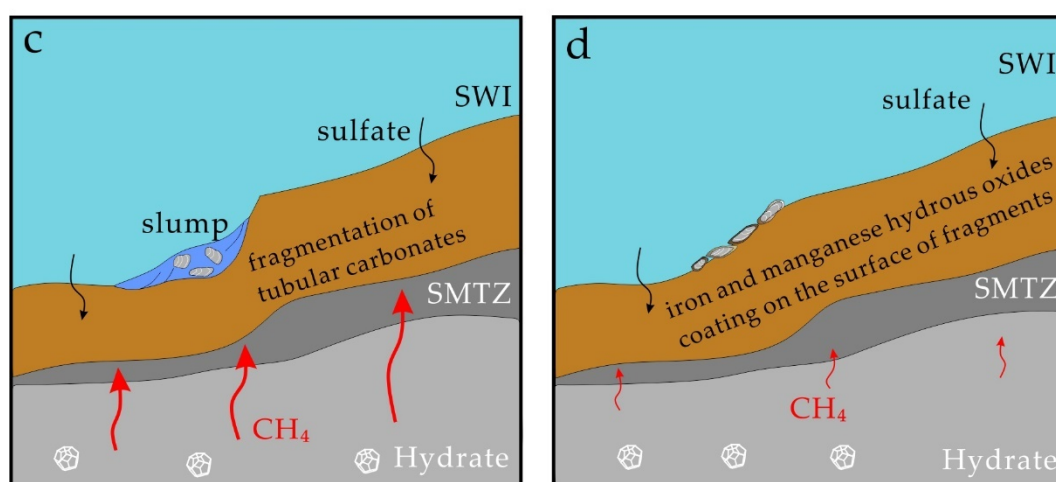


Figure 7. Cont.



**Figure 7.** A conceptual model for the formation of the tubular carbonates from the northern South China Sea (not to scale). (a) Active methane seepage occurred in the passive margin setting. Burrows produced by megafauna served as conduits for methane and sulfate flow. (b) The upward movement of the SMTZ placed burrows into the zone of anaerobic oxidation of methane (AOM), which resulted in the lithification of the surrounding sediments and carbonate cement precipitation within the inner parts of the conduits. (c) Turbidity currents and sediment slumps and slides caused the fragmentation of tubular carbonates. The overlying sediments were then eroded by the strong bottom currents. (d) Iron and manganese hydroxides coated the surface of carbonates during prolonged exposure of pipe fragments to oxic seawater (Figure 7d). SWI = sediment water interface, SMTZ = sulfate methane transition zone.

## 6. Conclusions

A pervasive occurrence of tubular carbonate was discovered in the Dongsha area of the South China Sea. Based on the morphology,  $\delta^{13}\text{C}_{\text{carb}}$  and  $\delta^{18}\text{O}_{\text{carb}}$  values, and trace and REE patterns of the samples, the carbonates pipes are inferred to have formed within the host sediment under anoxic conditions. The tubular carbonates probably resulted from the lithification of burrows generated by seep-dwelling megafauna such as crustaceans or bivalves. Biogenic methane, derived from hydrate decomposition during sea level lowstands, was apparently the dominant carbon source of carbonates. The tubular carbonates were fragmented by mass-wasting processes or the vigorous emission of fluids. This study elucidated the formation mode of a new mass occurrence of fragmented tubular carbonates, highlighting the combined effect of burrowing, sediment movement, and bottom currents on their formation.

**Supplementary Materials:** The following are available online at <http://www.mdpi.com/2075-163X/10/9/768/s1>. Figure S1: Plot of Mn, Fe, and rare earth element contents ( $\mu\text{g/g}$ ) of carbonate phase; Figure S2: Correlation diagrams between  $\text{Ce/Ce}^*$  and  $\text{Dy}_\text{N}/\text{Sm}_\text{N}$  (a), and total REE (b); Table S1:  $\delta^{13}\text{C}$  and  $\delta^{18}\text{O}$  values of carbonates.

**Author Contributions:** Conceptualization: D.F. and Y.S.; methodology: Y.S.; formal analysis: Y.S., J.P., Y.H., X.W., S.G., and Y.P.; investigation: Y.S.; resources: D.F.; data curation: Y.S.; writing—original draft preparation: Y.S., J.P., D.C., and D.F.; writing—review and editing: Y.S., J.P., and D.F.; visualization: Y.S.; supervision: D.F.; project administration: D.F.; funding acquisition: D.F. All authors have read and agreed to the published version of the manuscript.

**Funding:** The research was partially supported by the Qingdao National Laboratory for Marine Science and Technology (Grant: QNLM2016ORP0204), National Program on Global Change and Air-Sea Interaction (Grant no: GASI-GEOGE-05-04,) and the NSF of China (Grants: 41773091 and 41730528).

**Acknowledgments:** We express our sincere appreciation for the crews of the ROPOS and *Tan Kah Kee* Cruises for their professionalism in sampling. We are grateful to M. Jin, N. Li (both SCSIO), and A.T. Xu (GEOMAR) for their useful suggestions. Y.S. acknowledges the China Scholarship Council for supporting a research visit to Universität Hamburg. Insightful comments by the editor and two anonymous reviewers helped to improve the manuscript.

**Conflicts of Interest:** The authors declare no conflict of interest.

## References

1. Suess, E. Marine Cold Seeps: Background and Recent Advances. In *Hydrocarbons, Oils and Lipids: Diversity, Origin, Chemistry and Fate*; Wilkes, H., Ed.; Springer International Publishing: Berlin, Germany, 2018; pp. 1–21.
2. Boetius, A.; Ravensschlag, K.; Schubert, C.J.; Rickert, D.; Widdel, F.; Gieseke, A.; Amann, R.; Jørgensen, B.B.; Witte, U.; Pfannkuche, O. A marine microbial consortium apparently mediating anaerobic oxidation of methane. *Nature* **2000**, *407*, 623–626. [[CrossRef](#)] [[PubMed](#)]
3. Peckmann, J.; Thiel, V. Carbon cycling at ancient methane-seeps. *Chem. Geol.* **2004**, *205*, 443–467. [[CrossRef](#)]
4. Bohrmann, G.; Greinert, J.; Suess, E.; Torres, M. Authigenic carbonates from the Cascadia subduction zone and their relation to gas hydrate stability. *Geology* **1998**, *7*, 647–650. [[CrossRef](#)]
5. Michaelis, W.; Seifert, R.; Nauhaus, K.; Treude, T.; Thiel, V.; Blumenberg, M.; Knittel, K.; Gieseke, A.; Peterknecht, K.; Pape, T.; et al. Microbial reefs in the Black Sea fueled by anaerobic oxidation of methane. *Science* **2002**, *297*, 1013–1015. [[CrossRef](#)]
6. Campbell, K.A. Hydrocarbon seep and hydrothermal vent paleoenvironments and paleontology: Past developments and future research directions. *Paleogeogr. Paleoclimatol. Paleocol.* **2006**, *232*, 362–407. [[CrossRef](#)]
7. De Boever, E.; Birgel, D.; Thiel, V.; Muchez, P.; Peckmann, J.; Dimitrov, L.; Swennen, R. The formation of giant tubular concretions triggered by anaerobic oxidation of methane as revealed by archaeal molecular fossils (Lower Eocene, Varna, Bulgaria). *Paleogeogr. Paleoclimatol. Paleocol.* **2009**, *280*, 23–36. [[CrossRef](#)]
8. Bayon, G.; Dupré, S.; Ponzevera, E.; Etoubleau, J.; Chéron, S.; Pierre, C.; Mascle, J.; Boetius, A.; de Lange, G.J. Formation of carbonate chimneys in the Mediterranean Sea linked to deep-water oxygen depletion. *Nat. Geosci.* **2013**, *6*, 755. [[CrossRef](#)]
9. Zwicker, J.; Smrzka, D.; Gier, S.; Goedert, J.L.; Peckmann, J. Mineralized conduits are part of the uppermost plumbing system of Oligocene methane-seep deposits, Washington State (USA). *Mar. Petrol. Geol.* **2015**, *66*, 616–630. [[CrossRef](#)]
10. Tamborrino, L.; Himmler, T.; Elvert, M.; Conti, S.; Gualtieri, A.F.; Fontana, D.; Bohrmann, G. Formation of tubular carbonate conduits at Athina mud volcano, eastern Mediterranean Sea. *Mar. Petrol. Geol.* **2019**, *107*, 20–31. [[CrossRef](#)]
11. Díaz-del-Río, V.; Somoza, L.; Martínez-Frias, J.; Mata, M.P.; Delgado, A.; Hernandez-Molina, F.J.; Lunar, R.; Martín-Rubí, J.; Maestro, A.; Fernández-Puga, M. Vast fields of hydrocarbon-derived carbonate chimneys related to the accretionary wedge/olistostrome of the Gulf of Cádiz. *Mar. Geol.* **2003**, *195*, 177–200. [[CrossRef](#)]
12. León, R.; Somoza, L.; Medialdea, T.; González, F.; Díaz-del-Río, V.; Fernández-Puga, M.; Maestro, A.; Mata, M. Sea-floor features related to hydrocarbon seeps in deepwater carbonate-mud mounds of the Gulf of Cádiz: From mud flows to carbonate precipitates. *Geo-Mar. Lett.* **2007**, *27*, 237–247. [[CrossRef](#)]
13. Merinero, R.; Lunar, R.; Martínez-Frías, J.; Somoza, L.; Díaz-del-Río, V. Iron oxyhydroxide and sulphide mineralization in hydrocarbon seep-related carbonate submarine chimneys, Gulf of Cadiz (SW Iberian Peninsula). *Mar. Petrol. Geol.* **2008**, *25*, 706–713. [[CrossRef](#)]
14. Nyman, S.L.; Nelson, C.S.; Campbell, K.A. Miocene tubular concretions in East Coast Basin, New Zealand: Analogue for the subsurface plumbing of cold seeps. *Mar. Geol.* **2010**, *272*, 319–336. [[CrossRef](#)]
15. Angeletti, L.; Canese, S.; Franchi, F.; Montagna, P.; Reitner, J.; Walliser, E.O.; Taviani, M. The “chimney forest” of the deep Montenegrin margin, south-eastern Adriatic Sea. *Mar. Petrol. Geol.* **2015**, *66*, 542–554. [[CrossRef](#)]
16. Magalhães, V.H.; Pinheiro, L.M.; Ivanov, M.K.; Kozlova, E.; Blinova, V.; Kolganova, J.; Vasconcelos, C.; McKenzie, J.A.; Bernasconi, S.M.; Kopf, A.J.; et al. Formation processes of methane-derived authigenic carbonates from the Gulf of Cadiz. *Sediment. Geol.* **2012**, *243–244*, 155–168. [[CrossRef](#)]
17. Bohrmann, G.; Abegg, F.; Bahr, A.; Bergenthal, M.; Brüning, M.; Brinkmann, F.; Dentrecolas, S.; Franke, P.; Gassner, A.; Hessler, S.; et al. Report and Preliminary Results of R/V METEOR Cruise M70/3, Iraklion–Iraklion, 21 November–8 December, 2006. Cold Seeps of the Anaximander Mountains/Eastern Mediterranean. In *Berichte, Fachbereich Geowissenschaften*; Universität Bremen: Bremen, Germany, 2008; Available online: <https://media.suub.uni-bremen.de/bitstream/elib/4074/1/00010635.pdf> (accessed on 29 August 2008).
18. Haas, A.; Little, C.T.S.; Sahling, H.; Bohrmann, G.; Himmler, T.; Peckmann, J. Mineralization of vestimentiferan tubes at methane seeps on the Congo deep-sea fan. *Deep Sea Res. Part I Oceanogr. Res. Pap.* **2009**, *56*, 283–293. [[CrossRef](#)]

19. Suess, E. *FS Sonne Fahrtbericht/Cruise Report So177 Siger 2004, South China Sea Continental Margin: Geological Methane Budget and Environmental Effects of Methane Emissions and Gas Hydrates*; IFM-GEOMAR: Kiel, Germany, 2005.
20. Han, X.; Yang, K.; Huang, Y. Origin and nature of cold seep in northeastern Dongsha area, South China Sea: Evidence from chimney-like seep carbonates. *Chin. Sci. Bull.* **2013**, *58*, 3689–3697. [[CrossRef](#)]
21. Guan, H.; Sun, Y.; Zhu, X.; Mao, S.; Feng, D.; Wu, N.; Chen, D. Factors controlling the types of microbial consortia in cold-seep environments: A molecular and isotopic investigation of authigenic carbonates from the South China Sea. *Chem. Geol.* **2013**, *354*, 55–64. [[CrossRef](#)]
22. Taylor, B.; Hayes, D.E. The Tectonic Evolution of the South China Basin. In *The Tectonic and Geologic Evolution of Southeast Asian Seas and Islands*; Hayes, D.E., Ed.; American Geophysical Union: Washington, DC, USA, 1980; Volume 23, pp. 89–104.
23. Pang, X.; Yang, S.; Zhu, M.; Li, J. Deep-water fan systems and petroleum resources on the northern slope of the South China Sea. *Acta Geol. Sinica* **2004**, *78*, 626–631.
24. Yan, P.; Wang, Y.; Liu, J.; Zhong, G.; Liu, X. Discovery of the southwest Dongsha Island mud volcanoes amid the northern margin of the South China Sea. *Mar. Petrol. Geol.* **2017**, *88*, 858–870. [[CrossRef](#)]
25. Liu, B.; Song, H.; Guan, Y.; Liu, Y.; Chen, J.; Geng, M. Characteristics and formation mechanism of cold seep system in the northeastern continental slope of South China Sea from sub-bottom profiler data. *Chin. J. Geophys.* **2015**, *58*, 247–256. (In Chinese)
26. Li, L.; Liu, H.; Zhang, X.; Lei, X.; Sha, Z. BSRs, estimated heat flow, hydrate-related gas volume and their implications for methane seepage and gas hydrate in the Dongsha region, northern South China Sea. *Mar. Petrol. Geol.* **2015**, *67*, 785–794. [[CrossRef](#)]
27. Zhang, G.; Liang, J.; Lu, J.A.; Yang, S.; Zhang, M.; Holland, M.; Schultheiss, P.; Su, X.; Sha, Z.; Xu, H.; et al. Geological features, controlling factors and potential prospects of the gas hydrate occurrence in the east part of the Pearl River Mouth Basin, South China Sea. *Mar. Petrol. Geol.* **2015**, *67*, 356–367. [[CrossRef](#)]
28. Chen, D.F.; Huang, Y.Y.; Yuan, X.L.; Cathles, L.M. Seep carbonates and preserved methane oxidizing archaea and sulfate reducing bacteria fossils suggest recent gas venting on the seafloor in the Northeastern South China Sea. *Mar. Petrol. Geol.* **2005**, *22*, 613–621. [[CrossRef](#)]
29. Han, X.; Suess, E.; Huang, Y.; Wu, N.; Bohrmann, G.; Su, X.; Eisenhauer, A.; Rehder, G.; Fang, Y. Jiulong methane reef: Microbial mediation of seep carbonates in the South China Sea. *Mar. Geol.* **2008**, *249*, 243–256. [[CrossRef](#)]
30. Feng, D.; Qiu, J.-W.; Hu, Y.; Peckmann, J.; Guan, H.; Tong, H.; Chen, C.; Chen, J.; Gong, S.; Li, N.; et al. Cold seep systems in the South China Sea: An overview. *J. Asian Earth Sci.* **2018**, *168*, 3–16. [[CrossRef](#)]
31. Liu, Z.; Colin, C.; Li, X.; Zhao, Y.; Tuo, S.; Chen, Z.; Siringan, F.P.; Liu, J.T.; Huang, C.-Y.; You, C.-F.; et al. Clay mineral distribution in surface sediments of the northeastern South China Sea and surrounding fluvial drainage basins: Source and transport. *Mar. Geol.* **2010**, *277*, 48–60. [[CrossRef](#)]
32. Shao, L.; Li, X.; Geng, J.; Pang, X.; Lei, Y.; Qiao, P.; Wang, L.; Wang, H. Deep water bottom current deposition in the northern South China Sea. *Sci. China Ser. D Earth Sci.* **2007**, *50*, 1060–1066. [[CrossRef](#)]
33. Gong, C.; Wang, Y.; Peng, X.; Li, W.; Qiu, Y.; Xu, S. Sediment waves on the South China Sea Slope off southwestern Taiwan: Implications for the intrusion of the Northern Pacific Deep Water into the South China Sea. *Mar. Petrol. Geol.* **2012**, *32*, 95–109. [[CrossRef](#)]
34. Lüdmann, T.; Wong, H.K.; Berglar, K. Upward flow of North Pacific Deep Water in the northern South China Sea as deduced from the occurrence of drift sediments. *Geophys. Res. Lett.* **2005**, *32*. [[CrossRef](#)]
35. Xia, H.; Liu, Y.; Yang, Y. Internal-wave characteristics of strong bottom currents at the sand-wave zone of the northern South China Sea and its role in sand-wave motion. *J. Trop. Oceanogr.* **2009**, *28*, 15–22. (In Chinese)
36. Xu, Z.; Liu, K.; Yin, B.; Zhao, Z.; Wang, Y.; Li, Q. Long-range propagation and associated variability of internal tides in the South China Sea. *J. Geophys. Res. Oceans* **2016**, *121*, 8268–8286. [[CrossRef](#)]
37. Zhao, Z. Internal tide radiation from the Luzon Strait. *J. Geophys. Res. Oceans* **2014**, *119*, 5434–5448. [[CrossRef](#)]
38. Xie, X.; Liu, Q.; Zhao, Z.; Shang, X.; Cai, S.; Wang, D.; Chen, D. Deep sea currents driven by breaking internal tides on the continental slope. *Geophys. Res. Lett.* **2018**, *45*, 6160–6166. [[CrossRef](#)]
39. Thorpe, S.A.; White, M. A deep intermediate nepheloid layer. *Deep Sea Res. Part A. Oceanogr. Res. Pap.* **1988**, *35*, 1665–1671. [[CrossRef](#)]
40. Taylor, S.R.; McLennan, S.M. *The Continental Crust: Its Composition and Evolution*; Blackwell: Oxford, UK, 1985; p. 312.

41. Bau, M.; Dulski, P. Distribution of yttrium and rare-earth elements in the Penge and Kuruman iron-formations, Transvaal Supergroup, South Africa. *Precambrian Res.* **1996**, *79*, 37–55. [[CrossRef](#)]
42. Gong, S.; Hu, Y.; Li, N.; Feng, D.; Liang, Q.; Tong, H.; Peng, Y.; Tao, J.; Chen, D. Environmental controls on sulfur isotopic compositions of sulfide minerals in seep carbonates from the South China Sea. *J. Asian Earth Sci.* **2018**, *168*, 96–105. [[CrossRef](#)]
43. Yang, K.; Chu, F.; Ye, L.; Zhang, W.; Xu, D.; Zhu, J.; Yang, H. Implication of methane seeps from sedimentary geochemical proxies (Sr/Ca & Mg/Ca) in the northern South China Sea. *J. Jilin Univ. (Earth Sci. Ed.)* **2014**, *44*, 469–479. (In Chinese)
44. Ge, L.; Jiang, S.Y. Sr isotopic compositions of cold seep carbonates from the South China Sea and the Panoche Hills (California, USA) and their significance in palaeoceanography. *J. Asian Earth Sci.* **2013**, *65*, 34–41. [[CrossRef](#)]
45. Bayon, G.; Birot, D.; Ruffine, L.; Caprais, J.C.; Ponzevera, E.; Bollinger, C.; Donval, J.P.; Charlou, J.L.; Voisset, M.; Grimaud, S. Evidence for intense REE scavenging at cold seeps from the Niger Delta margin. *Earth Planet. Sci. Lett.* **2011**, *312*, 443–452. [[CrossRef](#)]
46. Freslon, N.; Bayon, G.; Toucanne, S.; Bermell, S.; Bollinger, C.; Chéron, S.; Etoubleau, J.; Germain, Y.; Khripounoff, A.; Ponzevera, E.; et al. Rare earth elements and neodymium isotopes in sedimentary organic matter. *Geochem. Cosmochim. Acta* **2014**, *140*, 177–198. [[CrossRef](#)]
47. Nozaki, Y. Rare Earth Elements and their Isotopes in the Ocean. In *Encyclopedia of Ocean Sciences*; Steele, J.H., Ed.; Academic Press: Oxford, UK, 2001; pp. 2354–2366. [[CrossRef](#)]
48. Nothdurft, L.D.; Webb, G.E.; Kamber, B.S. Rare earth element geochemistry of Late Devonian reefal carbonates, Canning Basin, Western Australia: Confirmation of a seawater REE proxy in ancient limestones. *Geochem. Cosmochim. Acta* **2004**, *68*, 263–283. [[CrossRef](#)]
49. Wang, Q.; Tong, H.; Huang, C.Y.; Chen, D. Tracing fluid sources and formation conditions of Miocene hydrocarbon-seep carbonates in the central Western Foothills, Central Taiwan. *J. Asian Earth Sci.* **2018**, *168*, 186–196. [[CrossRef](#)]
50. Hu, Y.; Feng, D.; Peckmann, J.; Roberts, H.H.; Chen, D.F. New insights into cerium anomalies and mechanisms of trace metal enrichment in authigenic carbonate from hydrocarbon seeps. *Chem. Geol.* **2014**, *381*, 55–66. [[CrossRef](#)]
51. Bayon, G.; Pierre, C.; Etoubleau, J.; Voisset, M.; Cauquil, E.; Marsset, T.; Sultan, N.; Le Drezen, E.; Fouquet, Y. Sr/Ca and Mg/Ca ratios in Niger Delta sediments: Implications for authigenic carbonate genesis in cold seep environments. *Mar. Geol.* **2007**, *241*, 93–109. [[CrossRef](#)]
52. Chen, F.; Hu, Y.; Feng, D.; Zhang, X.; Cheng, S.; Cao, J.; Lu, H.; Chen, D. Evidence of intense methane seepages from molybdenum enrichments in gas hydrate-bearing sediments of the northern South China Sea. *Chem. Geol.* **2016**, *443*, 173–181. [[CrossRef](#)]
53. Portilho-Ramos, R.C.; Cruz, A.P.S.; Barbosa, C.F.; Rathburn, A.E.; Mulitza, S.; Venancio, I.M.; Schwenk, T.; Ruehlemann, C.; Vidal, L.; Chiessi, C.M.; et al. Methane release from the southern Brazilian margin during the last glacial. *Sci. Rep.* **2018**, *8*, s41598-s018. [[CrossRef](#)]
54. León, R.; Somoza, L.; Medialdea, T.; González, F.J.; Gimenez-Moreno, C.J.; Pérez-López, R. Pockmarks on either side of the Strait of Gibraltar: Formation from overpressured shallow contourite gas reservoirs and internal wave action during the last glacial sea-level lowstand? *Geo-Mar. Lett.* **2014**, *34*, 131–151. [[CrossRef](#)]
55. Tong, H.; Feng, D.; Cheng, H.; Yang, S.; Wang, H.; Min, A.G.; Edwards, R.L.; Chen, Z.; Chen, D. Authigenic carbonates from seeps on the northern continental slope of the South China Sea: New insights into fluid sources and geochronology. *Mar. Petrol. Geol.* **2013**, *43*, 260–271. [[CrossRef](#)]
56. Oppo, D.; Capozzi, R.; Picotti, V.; Ponza, A. A genetic model of hydrocarbon-derived carbonate chimneys in shelfal fine-grained sediments: The Enza River field, Northern Apennines (Italy). *Mar. Petrol. Geol.* **2015**, *66*, 555–565. [[CrossRef](#)]
57. Aloisi, G.; Pierre, C.; Rouchy, J.-M.; Foucher, J.-P.; Woodside, J. Methane-related authigenic carbonates of eastern Mediterranean Sea mud volcanoes and their possible relation to gas hydrate destabilisation. *Earth Planet. Sci. Lett.* **2000**, *184*, 321–338. [[CrossRef](#)]
58. Lu, Y.; Xu, L.; Chen, T.; Sun, X.; Xu, H.; Konishi, H.; Hao, X.; Lin, Z.; Lu, H.; Peckmann, J. Formation of dolomite catalyzed by sulfate-driven anaerobic oxidation of methane: Mineralogical and geochemical evidence from the northern South China Sea. *Am. Mineral.* **2018**, *103*, 720–734. [[CrossRef](#)]

59. Han, X.; Suess, E.; Liebetrau, V.; Eisenhauer, A.; Huang, Y. Past methane release events and environmental conditions at the upper continental slope of the South China Sea: Constraints by seep carbonates. *Int. J. Earth Sci.* **2014**, *103*, 1873–1887. [[CrossRef](#)]
60. Zhuang, C.; Chen, F.; Cheng, S.; Lu, H.; Wu, C.; Cao, J.; Duan, X. Light carbon isotope events of foraminifera attributed to methane release from gas hydrates on the continental slope, northeastern South China Sea. *Sci. China Earth Sci.* **2016**, *59*, 1981–1995. [[CrossRef](#)]
61. Tarutani, T.; Clayton, R.N.; Mayeda, T.K. The effect of polymorphism and magnesium substitution on oxygen isotope fractionation between calcium carbonate and water. *Geochem. Cosmochim. Acta* **1969**, *33*, 987–996. [[CrossRef](#)]
62. Kim, S.T.; O’Neil, J.R. Equilibrium and nonequilibrium oxygen isotope effects in synthetic carbonates. *Geochem. Cosmochim. Acta* **1997**, *61*, 3461–3475. [[CrossRef](#)]
63. Feng, D.; Chen, D. Authigenic carbonates from an active cold seep of the northern South China Sea: New insights into fluid sources and past seepage activity. *Deep Sea Res. Part II Top. Stud. Oceanogr.* **2015**, *122*, 74–83. [[CrossRef](#)]
64. Franchi, F.; Rovere, M.; Gamberi, F.; Rashed, H.; Vaselli, O.; Tassi, F. Authigenic minerals from the Paola Ridge (southern Tyrrhenian Sea): Evidences of episodic methane seepage. *Mar. Petrol. Geol.* **2017**, *86*, 228–247. [[CrossRef](#)]
65. Feng, D.; Chen, D.; Peckmann, J. Rare earth elements in seep carbonates as tracers of variable redox conditions at ancient hydrocarbon seeps. *Terra Nova* **2009**, *21*, 49–56. [[CrossRef](#)]
66. Frimmel, H.E. Trace element distribution in Neoproterozoic carbonates as palaeoenvironmental indicator. *Chem. Geol.* **2009**, *258*, 338–353. [[CrossRef](#)]
67. Himmler, T.; Bach, W.; Bohrmann, G.; Peckmann, J. Rare earth elements in authigenic methane-seep carbonates as tracers for fluid composition during early diagenesis. *Chem. Geol.* **2010**, *277*, 126–136. [[CrossRef](#)]
68. Rongemaille, E.; Bayon, G.; Pierre, C.; Bollinger, C.; Chu, N.C.; Fouquet, Y.; Riboulot, V.; Voisset, M. Rare earth elements in cold seep carbonates from the Niger delta. *Chem. Geol.* **2011**, *286*, 196–206. [[CrossRef](#)]
69. Feng, D.; Chen, D.; Roberts, H.H. Petrographic and geochemical characterization of seep carbonate from Bush Hill (GC 185) gas vent and hydrate site of the Gulf of Mexico. *Mar. Petrol. Geol.* **2009**, *26*, 1190–1198. [[CrossRef](#)]
70. Argentino, C.; Lugli, F.; Cipriani, A.; Conti, S.; Fontana, D. A deep fluid source of radiogenic Sr and highly dynamic seepage conditions recorded in Miocene seep carbonates of the northern Apennines (Italy). *Chem. Geol.* **2019**, *522*, 135–147. [[CrossRef](#)]
71. Haley, B.A.; Klinkhammer, G.P.; McManus, J. Rare earth elements in pore waters of marine sediments. *Geochem. Cosmochim. Acta* **2004**, *68*, 1265–1279. [[CrossRef](#)]
72. Himmler, T.; Haley, B.A.; Torres, M.E.; Klinkhammer, G.P.; Bohrmann, G.; Peckmann, J. Rare earth element geochemistry in cold-seep pore waters of Hydrate Ridge, northeast Pacific Ocean. *Geo-Mar. Lett.* **2013**, *33*, 369–379. [[CrossRef](#)]
73. Moffett, J.W. Microbially mediated cerium oxidation in sea water. *Nature* **1990**, *345*, 421–423. [[CrossRef](#)]
74. Feng, D.; Chen, D.; Roberts, H.H. Sedimentary fabrics in the authigenic carbonates from Bush Hill: Implication for seabed fluid flow and its dynamic signature. *Geofluids* **2008**, *8*, 301–310. [[CrossRef](#)]
75. Feng, D.; Chen, D.; Peckmann, J.; Bohrmann, G. Authigenic carbonates from methane seeps of the northern Congo fan: Microbial formation mechanism. *Mar. Petrol. Geol.* **2010**, *27*, 748–756. [[CrossRef](#)]
76. De Boever, E.; Swennen, R.; Dimitrov, L. Lower Eocene carbonate cemented chimneys (Varna, NE Bulgaria): Formation mechanisms and the (a) biological mediation of chimney growth? *Sediment. Geol.* **2006**, *185*, 159–173. [[CrossRef](#)]
77. Peng, X.; Guo, Z.; Chen, S.; Sun, Z.; Xu, H.; Ta, K.; Zhang, J.; Zhang, L.; Li, J.; Du, M. Formation of carbonate pipes in the northern Okinawa Trough linked to strong sulfate exhaustion and iron supply. *Geochem. Cosmochim. Acta* **2017**, *205*, 1–13. [[CrossRef](#)]
78. Reitner, J.; Blumenberg, M.; Walliser, E.O.; Schäfer, N.; Duda, J.-P. Methane-derived carbonate conduits from the late Aptian of Salinac (Marne Bleues, Vocontian Basin, France): Petrology and biosignatures. *Mar. Petrol. Geol.* **2015**, *66*, 641–652. [[CrossRef](#)]
79. Wetzel, A. Formation of methane-related authigenic carbonates within the bioturbated zone—An example from the upwelling area off Vietnam. *Paleogeogr. Paleoclimatol. Paleoecol.* **2013**, *386*, 23–33. [[CrossRef](#)]

80. Wiese, F.; Kiel, S.; Pack, A.; Walliser, E.O.; Agirrezabala, L.M. The beast burrowed, the fluid followed –Crustacean burrows as methane conduits. *Mar. Petrol. Geol.* **2015**, *66*, 631–640. [[CrossRef](#)]
81. Bodin, S.; Rose, J.C. Hydrocarbon-seep carbonates associated with Mesozoic environmental perturbations: Example from the Lower Bajocian of Morocco. *Sediment. Geol.* **2018**, *374*, 53–68. [[CrossRef](#)]
82. van de Schootbrugge, B.; Harazim, D.; Sorichter, K.; Oschmann, W.; Fiebig, J.; Püttmann, W.; Peinl, M.; Zanella, F.; Teichert, B.; Hoffmann, J. The enigmatic ichnofossil *Tisosa siphonalis* and widespread authigenic seep carbonate formation during the Late Pliensbachian in southern France. *Biogeosciences* **2010**, *7*, 3123–3138. [[CrossRef](#)]
83. Paull, C.K.; Ussler, W.; Dallimore, S.R.; Blasco, S.M.; Lorenson, T.D.; Melling, H.; Medioli, B.E.; Nixon, F.M.; McLaughlin, F.A. Origin of pingo-like features on the Beaufort Sea shelf and their possible relationship to decomposing methane gas hydrates. *Geophys. Res. Lett.* **2007**, *34*. [[CrossRef](#)]
84. Cau, S.; Franchi, F.; Roveri, M.; Taviani, M. The Pliocene-age Stirone River hydrocarbon chemoherm complex (Northern Apennines, Italy). *Mar. Petrol. Geol.* **2015**, *66*, 582–595. [[CrossRef](#)]
85. González, F.; Somoza, L.; Lunar, R.; Martínez-Frías, J.; Rubí, J.M.; Torres, T.; Ortiz, J.; del Río, V.D.; Pinheiro, L.; Magalhães, V. Hydrocarbon-derived ferromanganese nodules in carbonate-mud mounds from the Gulf of Cadiz: Mud-breccia sediments and clasts as nucleation sites. *Mar. Geol.* **2009**, *261*, 64–81. [[CrossRef](#)]
86. González, F.; Somoza, L.; Lunar, R.; Martínez-Frías, J.; Rubí, J.M.; Torres, T.; Ortiz, J.; Díaz-del-Río, V. Internal features, mineralogy and geochemistry of ferromanganese nodules from the Gulf of Cadiz: The role of the Mediterranean Outflow Water undercurrent. *J. Mar. Syst.* **2010**, *80*, 203–218. [[CrossRef](#)]



© 2020 by the authors. Licensee MDPI, Basel, Switzerland. This article is an open access article distributed under the terms and conditions of the Creative Commons Attribution (CC BY) license (<http://creativecommons.org/licenses/by/4.0/>).